

Spartus: A 9.4 TOP/s FPGA-based LSTM Accelerator Exploiting Spatio-Temporal Sparsity

Chang Gao, *Member, IEEE*, Tobi Delbruck, *Fellow, IEEE* and Shih-Chii Liu, *Fellow, IEEE*

Abstract—Long Short-Term Memory (LSTM) recurrent networks are frequently used for tasks involving time-sequential data such as speech recognition. Unlike previous LSTM accelerators that either exploit spatial weight sparsity or temporal activation sparsity, this paper proposes a new accelerator called “Spartus” that exploits spatio-temporal sparsity to achieve ultra-low latency inference. Spatial sparsity is induced using a new Column-Balanced Targeted Dropout (CBTD) structured pruning method, producing structured sparse weight matrices for a balanced workload. The pruned networks running on Spartus hardware achieve weight sparsity levels of up to 96% and 94% with negligible accuracy loss on the TIMIT and the Librispeech datasets. To induce temporal sparsity in LSTM, we extend the previous DeltaGRU method to the DeltaLSTM method. Combining spatio-temporal sparsity with CBTD and DeltaLSTM saves on weight memory access and associated arithmetic operations. The Spartus architecture is scalable and supports real-time online speech recognition when implemented on small and large FPGAs. Spartus per-sample latency for a single DeltaLSTM layer of 1024 neurons averages 1 μ s. Exploiting spatio-temporal sparsity on our test LSTM network using the TIMIT dataset leads to 46 \times speedup of Spartus over its theoretical hardware performance to achieve 9.4 TOP/s effective batch-1 throughput and 1.1 TOP/s/W power efficiency.

Index Terms—recurrent neural network, structured pruning, delta network, edge computing, spiking neural network, dropout

I. INTRODUCTION

RECURRENT Neural Networks (RNNs) are widely used in tasks that involve temporal sequences. RNN variants such as the Long Short-Term Memory (LSTM) [1] and Gated Recurrent Unit (GRU) [2] models use additional gating units to mitigate the problem of vanishing gradient. These variants achieve state-of-the-art prediction accuracy in tasks involving input temporal sequences such as automatic speech recognition [3], [4], and natural language processing [5]. RNNs are also useful in latency-critical real-time control tasks, such as robotic prosthesis control [6], gaming AI [7] and autonomous driving [8], which require the hardware to maintain high throughput even with a batch size of one input sample.

Batch-1 RNN calculation is dominated by Matrix-Vector Multiplication (MxV) since there is only one input stream and the fetched big weight matrix cannot be shared across multiple

C. Gao, T. Delbruck and S-C. Liu are with the Sensors Group at the Institute of Neuroinformatics, University of Zurich and ETH Zurich, Zurich (sensors.ini.uzh.ch), Switzerland, 8057 Switzerland (email: chang@ini.uzh.ch; shih@ini.uzh.ch; tobi@ini.uzh.ch).

This work was supported by Samsung Advanced Institute of Technology (SAIT) Global Research *Neuromorphic Processor* project, the Swiss National Competence Center in Robotics (NCCR Robotics, 51NF40_185543), and the Swiss National Science Foundation BRIDGE project VIPS (181010).

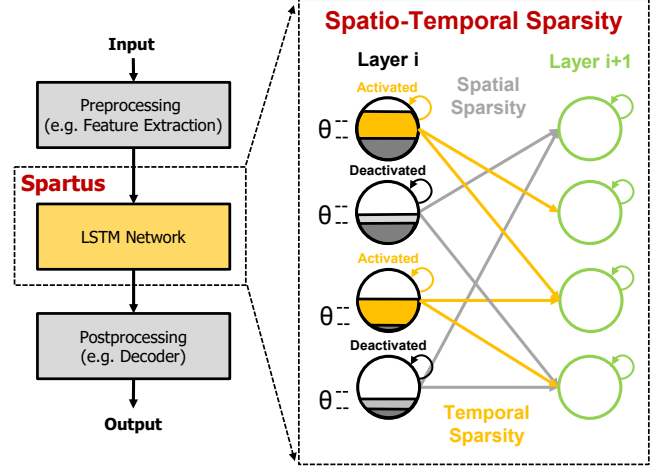


Fig. 1: Concept of the Spartus accelerator that exploits spatio-temporal sparsity on layer i of a multi-layer LSTM network. The structured spatial sparsity ensures an equal number of outward connections between units in layer i for a balanced workload. The change of activations (yellow) can be either positive or negative.

input streams. The computational cost of this calculation grows quadratically with a linear increase in RNN units. The reasons why it is difficult to achieve low cost, latency, and power simultaneously for RNN hardware inference are fourfold. First, the temporal dependence between the current and previous network output creates a critical path that limits the parallelism between time steps. Second, large networks are essential for high accuracy, leading to a large memory footprint that is expensive to buffer on-chip. Third, MxV is a memory-bounded operation, and the available memory bandwidth limits the minimum latency to fetch the large weight matrices. Fourth, memory access consumes at least 10 \times more energy than arithmetic operations with the same number of bits [9], [10]. In short, the key to achieving low-cost, low-latency, low-power RNN inference is to reduce the memory bottleneck, that is, to minimize the needed access of weights.

A popular method to reduce memory access is to sparsify the weight matrices. Pruning methods [11]–[13] remove unimportant connections between neurons, resulting in sparse weight matrices with a smaller memory footprint than the original dense matrices. Structured pruning was later introduced in RNN accelerators to address the problem of workload imbalance caused by irregular weight sparsity patterns after pruning [14]–[17]. The Bank Balanced Sparsity (BBS) [15] method

divides the rows of a weight matrix into banks of equal length. Then, fine-grain pruning is applied to each bank with an equal number of nonzero elements in each bank. The Hierarchical Coarse-Grain Sparsity (HCGS) structured pruning method pre-partitions the weight matrix with hierarchical levels of squared submatrices and removes equal numbers of weight elements in each submatrix to ensure a balanced workload. This method was used in a recent power-efficient Application Specific Integrated Circuit (ASIC) Recurrent Neural Network (RNN) accelerator [17]. Structured weight matrices can also reduce the effective number of weights and MxV cost without increasing sparsity: Block-circulant matrices enable the use of the fast Fourier transform to reduce the cost of MxV from $\mathcal{O}(n^2)$ to $\mathcal{O}(n \log(n))$ [18]–[20].

Another way to reduce memory access requirements is to increase the temporal sparsity of activations, as in spiking neural networks. The Delta Network (DN) algorithm was inspired by the neuromorphic principle that neurons have sparse activity transmission and introduced as a method to induce temporal sparsity in deep networks by replacing state vectors with delta vectors that contain the deltas of the temporal difference of the states between two adjacent time steps [21]. Zeroing deltas that are below a delta threshold produces sparse delta vectors. Using these sparsified delta vectors results in an insignificant accuracy loss if the RNN is properly trained. Using hardware that can skip zeros in delta state vectors, we can remove operations from entire columns of the weight matrix, which is intrinsically workload balanced [22], [23]. Temporal sparsity is similar to activation sparsity, and to our best knowledge, it was only exploited in 3 previous hardware accelerator works on Convolutional Neural Networks (CNN) [24], [25] and RNNs [22].

Finally, quantization of weights and states [26] can be combined with the previous sparsity-inducing methods to reduce the model size further. In the basic DN algorithm, columns of weights that are not skipped are still dense. There is an opportunity to further reduce the memory footprint by inducing weight sparsity in a delta RNN. However, it is challenging to implement efficiently because the hardware has to deal with the irregular sparsity pattern in both delta state vectors and weight matrices. Previous RNN hardware accelerators only exploited either spatial sparsity [12], [15], [16], [19], [20] or temporal sparsity [22], [23]. It is challenging to exploit both sparsity types simultaneously because the hardware has to deal with the static sparsity pattern in weights and the dynamic sparsity pattern in states simultaneously. Our paper describes an accelerator that achieves a further speedup of LSTM RNN inference by exploiting spatio-temporal sparsity in both weights and states of the network, as shown in Fig. 1. The main contributions of this work are:

- 1) We extend the delta network algorithm [21] to LSTM to propose Delta Long-Short Term Memory (**DeltaLSTM**), inducing temporal sparsity in LSTM networks (Sec. II).
- 2) We introduce a structured pruning method called Column-Balanced Targeted Dropout (**CBTD**)¹ that produces a balanced workload among columns of a weight matrix

(Sec. III-A). CBTD achieves up to 96% and 94% weight sparsity of an LSTM network without accuracy loss, respectively, on the TIMIT and the large-scale Librispeech datasets. By comparison with the hardware-optimized HCGS pruning method [17], CBTD achieves 10 \times lower accuracy loss on Librispeech (Sec. VI-B).

- 3) We present the first hardware LSTM-RNN accelerator, **Spartus**, that exploits both spatial and temporal sparsity in LSTM (Sec. IV). The LSTM weight matrices are encoded in our customized sparse matrix format called Column-Balanced Compressed Sparse Column (**CBCSC**) that can be efficiently processed by the hardware (Sec. III-C).
- 4) **Spartus** is reconfigurable in the number of arithmetic Processing Elements (**PE**) and thus can be easily implemented on various sizes of Field Programmable Gate Arrays (**FPGA**) (Sec. IV-D). Evaluated on the TIMIT dataset, **Spartus** on the largest Xilinx Zynq FPGA achieves 1 μ s inference latency of an LSTM layer with 4.7 million parameters, 9.4 TOP/s effective batch-1 throughput, and 1.1 TOP/J effective power efficiency. In comparison to previous RNN accelerators (Sect. VII-A), the **Spartus** throughput and power efficiency are respectively 4 \times and 7 \times higher than previous state-of-the-art FPGA accelerators BBS [15] and DeltaRNN [22] (Sec. VII-A). **Edge-Spartus** on the smallest Zynq FPGA achieves 33.6 GOp/s/W effective power efficiency, which is 4 \times higher than the previous EdgeDRNN [23] accelerator that only exploited temporal sparsity (Sec. VII-B), and **Edge-Spartus** uses inexpensive external memory to run even the largest networks.

II. LSTM & DELTALSTM NETWORKS

This section introduces the background of the LSTM networks and describes our proposed variant architecture of LSTM called DeltaLSTM to realize efficient LSTM inference.

A. LSTM

An LSTM unit is composed of an input gate **i**, a forget gate **f**, a cell gate **g**, an output gate **o**, and a memory cell state **c**. Gates **i**, **f**, **g** control the update of the cell **c** state. Gate **o** determines the proportion of cell memory that is transferred to the hidden state output **h**. In an LSTM layer, each gate receives two input sequences of length T , including an input sequence $X = \{\mathbf{x}_t | 1 \leq t \leq T, t \in \mathbb{N}\}$ and a sequence of previous hidden states $H_{in} = \{\mathbf{h}_t | 0 \leq t \leq T-1, t \in \mathbb{N}\}$ from the unit itself. At each time step, the LSTM layer generates a new hidden state vector, giving a sequence $H_{out} = \{\mathbf{h}_t | 1 \leq t \leq T, t \in \mathbb{N}\}$.

The formulations of an LSTM layer are given as:

$$\begin{aligned}
 \mathbf{i}_t &= \sigma(\mathbf{W}_{ii}\mathbf{x}_t + \mathbf{b}_{ii} + \mathbf{W}_{hi}\mathbf{h}_{t-1} + \mathbf{b}_{hi}) \\
 \mathbf{f}_t &= \sigma(\mathbf{W}_{if}\mathbf{x}_t + \mathbf{b}_{if} + \mathbf{W}_{hf}\mathbf{h}_{t-1} + \mathbf{b}_{hf}) \\
 \mathbf{g}_t &= \tanh(\mathbf{W}_{ig}\mathbf{x}_t + \mathbf{b}_{ig} + \mathbf{W}_{hg}\mathbf{h}_{t-1} + \mathbf{b}_{hg}) \\
 \mathbf{o}_t &= \sigma(\mathbf{W}_{io}\mathbf{x}_t + \mathbf{b}_{io} + \mathbf{W}_{ho}\mathbf{h}_{t-1} + \mathbf{b}_{ho}) \\
 \mathbf{c}_t &= \mathbf{f}_t \odot \mathbf{c}_{t-1} + \mathbf{i}_t \odot \mathbf{g}_t \\
 \mathbf{h}_t &= \mathbf{o}_t \odot \tanh(\mathbf{c}_t)
 \end{aligned} \tag{1}$$

¹<https://github.com/gaochangw/DeltaLSTM-CBTD>

where W denotes weight matrices, b denotes bias vectors, and σ denotes the logistic sigmoid function. The symbol \odot signifies pointwise multiplication.

B. DeltaLSTM

The DeltaLSTM can be understood as follows. Given an input sequence, $X = \{\mathbf{x}_t | 1 \leq t \leq T, t \in \mathbb{N}\}$, the output is given by $Y = \{\mathbf{y}_t | 1 \leq t \leq T, t \in \mathbb{N}\}$:

$$\begin{aligned} \mathbf{y}_t &= \mathbf{W}\mathbf{x}_t \\ \mathbf{y}_t &= \mathbf{W}\Delta\mathbf{x}_t + \mathbf{y}_{t-1} \end{aligned} \quad (2)$$

where $\Delta\mathbf{x}_t = \mathbf{x}_t - \mathbf{x}_{t-1}$ is the difference between the input sequence elements from adjacent time steps and is called a delta vector. \mathbf{W} is the matrix of weight connections from the input to the neurons. The delta vector can be sparse if all its elements below a delta threshold Θ are set to zero; thus, the term $\mathbf{W}\Delta\mathbf{x}$ in Eq. (2) becomes a dense matrix - sparse vector multiplication, in which Multiply-Accumulate (MAC) operations in matrix columns that correspond to zero delta vector elements can be skipped to reduce weight memory access.

The DN algorithm was only studied and implemented as Delta Gated Recurrent Unit (**DeltaGRU**). The DeltaLSTM extends the DN algorithm to LSTM RNNs. Using (2), the LSTM equations (1) are converted to the DeltaLSTM equations following the formulations in (3):

$$\begin{aligned} \mathbf{i}_t &= \sigma(\mathbf{D}_{i,t}) = \sigma(\mathbf{W}_{ii}\Delta\mathbf{x}_t + \mathbf{W}_{hi}\Delta\mathbf{h}_{t-1} + \mathbf{D}_{i,t-1}) \\ \mathbf{f}_t &= \sigma(\mathbf{D}_{f,t}) = \sigma(\mathbf{W}_{if}\Delta\mathbf{x}_t + \mathbf{W}_{hf}\Delta\mathbf{h}_{t-1} + \mathbf{D}_{f,t-1}) \\ \mathbf{g}_t &= \tanh(\mathbf{D}_{g,t}) = \tanh(\mathbf{W}_{ig}\Delta\mathbf{x}_t + \mathbf{W}_{hg}\Delta\mathbf{h}_{t-1} + \mathbf{D}_{g,t-1}) \\ \mathbf{o}_t &= \sigma(\mathbf{D}_{o,t}) = \sigma(\mathbf{W}_{io}\Delta\mathbf{x}_t + \mathbf{W}_{ho}\Delta\mathbf{h}_{t-1} + \mathbf{D}_{o,t-1}) \\ \mathbf{c}_t &= \mathbf{f}_t \odot \mathbf{c}_{t-1} + \mathbf{i}_t \odot \mathbf{g}_t \\ \mathbf{h}_t &= \mathbf{o}_t \odot \tanh(\mathbf{c}_t) \end{aligned} \quad (3)$$

where the terms \mathbf{D} denote the delta memory for each gate, and they are $M \times V$ results accumulated over time. The delta memory terms in DeltaLSTM at $t = 1$ correspond to the bias terms in the LSTM and are initialized to zeros. Because the delta threshold forces the partial elements of the delta vectors to be zeros, two vectors $\hat{\mathbf{x}}_{t-1}$ and $\hat{\mathbf{h}}_{t-2}$ are used to store the correct previous states to prevent accumulating errors in delta memories. Elements of $\hat{\mathbf{x}}_{t-1}$ and $\hat{\mathbf{h}}_{t-2}$ are updated only when their corresponding delta vector elements are above the delta threshold. The delta vector update process is defined by (4)~(7).

$$\Delta\mathbf{x}_t = \begin{cases} \mathbf{x}_t - \hat{\mathbf{x}}_{t-1} & , |\mathbf{x}_t - \hat{\mathbf{x}}_{t-1}| > \Theta \\ 0 & , |\mathbf{x}_t - \hat{\mathbf{x}}_{t-1}| \leq \Theta \end{cases} \quad (4)$$

$$\hat{\mathbf{x}}_{t-1} = \begin{cases} \mathbf{x}_{t-1} & , |\mathbf{x}_t - \hat{\mathbf{x}}_{t-1}| > \Theta \\ \hat{\mathbf{x}}_{t-2} & , |\mathbf{x}_t - \hat{\mathbf{x}}_{t-1}| \leq \Theta \end{cases} \quad (5)$$

$$\Delta\mathbf{h}_{t-1} = \begin{cases} \mathbf{h}_{t-1} - \hat{\mathbf{h}}_{t-2} & , |\mathbf{h}_{t-1} - \hat{\mathbf{h}}_{t-2}| > \Theta \\ 0 & , |\mathbf{h}_{t-1} - \hat{\mathbf{h}}_{t-2}| \leq \Theta \end{cases} \quad (6)$$

$$\hat{\mathbf{h}}_{t-2} = \begin{cases} \mathbf{h}_{t-2} & , |\mathbf{h}_{t-1} - \hat{\mathbf{h}}_{t-2}| > \Theta \\ \hat{\mathbf{h}}_{t-3} & , |\mathbf{h}_{t-1} - \hat{\mathbf{h}}_{t-2}| \leq \Theta \end{cases} \quad (7)$$

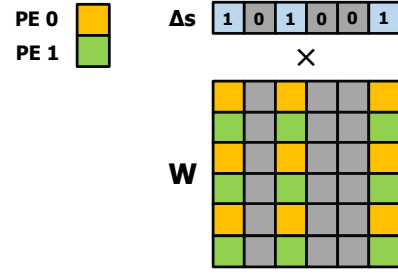


Fig. 2: Example of matrix-vector multiplication in Spartus between the weight matrix, \mathbf{W} , and the delta state vector, Δs . The workload assignment of 2 PEs is shown here. Skipped columns due to zeros in Δs are highlighted in gray.

The complete set of DeltaLSTM equations is formed by (3) and (4)~(7).

III. STRUCTURED PRUNING OF DELTALSTM

The DN algorithm converts dense-matrix-dense-vector multiplication in LSTM to dense-matrix-sparse-vector multiplication to save columns of $M \times V$ operations, but the remaining columns are still dense. These dense columns can be sparsified by pruning. However, random access of weight matrix columns is required to exploit temporal sparsity in delta state vectors and this leads to difficulties in further exploiting sparsity in weight columns; that is, parallelizing MAC operations for hardware PEs on remaining nonzero elements.

Although fine-grain pruning methods [11] could achieve high sparsity around 90% in RNN weights with negligible accuracy loss, they introduce irregular nonzero element distribution in the pruned sparse matrix leading to an unbalanced workload for PEs. Other structured pruning methods like BBS can create structured sparse weights, but the workload will not be balanced once combined with temporal DeltaLSTM. This is because the nonzero values are not evenly distributed across columns and will lead to an unbalanced workload when combined with temporal sparsity. In this work, we propose a hardware-oriented pruning method called CBTD that balances the workload even with the random weight column access in DeltaLSTM.

A. Column-Balanced Targeted Dropout (CBTD)

As shown in Fig. 2, interleaved rows of $M \times V$ workload are assigned to PEs that have MAC units for $M \times V$ computation in the Spartus accelerator. The procedure of applying CBTD on a weight matrix is shown in Algorithm 1. Given M , which is the number of PEs along the column direction in the Spartus accelerator, CBTD splits each column into the same number of groups (also called subcolumns) as the number of PEs. Thus, M determines the size of each subcolumn for an LSTM layer of a certain size. Next, weight elements in each subcolumn are sorted by their magnitudes. Then, the smallest $\lfloor H/M * \gamma \rfloor$ portion of elements in each subcolumn is set to zero with a dropout probability α and a target sparsity, γ . The α probability was used to introduce stochasticity in the targeted dropout process. The same γ and α are used for all

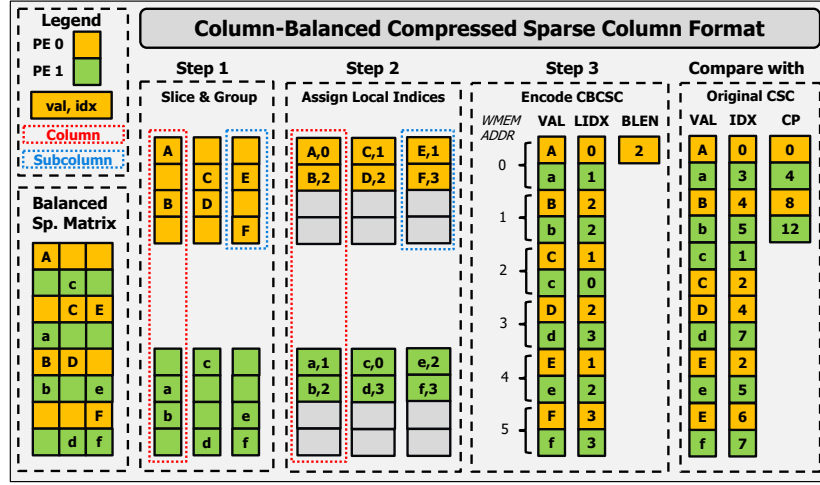


Fig. 3: Steps to encode a sparse matrix into the Column-Balanced Compressed Sparse Column (CBCSC) format

Algorithm 1: Column-Balanced Targeted Dropout (CBTD)

Data: \mathbf{A} , matrix;
 Q , the number of columns in \mathbf{A} ;
 H , the height of columns in \mathbf{A} ;
 γ , target sparsity;
 α , dropout probability;
 M , number of PEs allocated along a column.

Result: A sparse weight matrix \mathbf{B} of which columns having balanced workload for each PE;

Build set C containing all columns of \mathbf{A} , where
 $C = \{c_j | c_j \in \mathbb{R}^H, 1 \leq j \leq Q, j \in \mathbb{N}\}$;
Shuffle and split columns in set C into subcolumns
 $S = \{s_{ij} | s_{ij} \in \mathbb{R}^{H/M}, 1 \leq i \leq M, 1 \leq j \leq Q, i, j \in \mathbb{N}\}$;

for $j = 1$ **to** Q **do**
 for $i = 1$ **to** M **do**
 Sort elements of s_{ij} by their magnitudes;
 Set the smallest $\lfloor H/M * \gamma \rfloor$ elements in s_{ij} to zero with a probability of α ;
 end
end
Reverse the shuffling and splitting to build a sparse matrix \mathbf{B} from subcolumns in set S ;
return \mathbf{B}

subcolumns to ensure the same number of nonzero elements in each subcolumn. Therefore, M determines the granularity of CBTD. With a larger M , the locations of nonzero weights are more tightly constrained due to the smaller subcolumn size and vice versa.

B. LSTM Training with CBTD

CBTD is applied to the training procedure of LSTM networks as described in Algorithm 2. The CBTD is used to set relatively unimportant weights to zeros in each epoch after the parameter update step. Weights that are set to zero in the previous epoch are allowed to recover during the parameter update step in the next epoch. The target sparsity γ is fixed

Algorithm 2: LSTM Training with CBTD

Data: \mathbf{W} , LSTM weight matrices;
 Q , the number of columns in \mathbf{W} ;
 H , the height of columns in \mathbf{W} ;
 γ , target sparsity;
 α , dropout probability;
 $\Delta\alpha$, step size of dropout probability;
 M , number of PEs per column.

Result: Trained network with a sparse weight matrix in which columns have a balanced workload for each PE;

$\alpha = 0$;
for iterations **do**
 Forward Propagation;
 Backward Propagation;
 Update Parameters \mathbf{W} ;
 CBTD (\mathbf{W} , Q , H , γ , α , M);
 if $\alpha < 1$ **then**
 $\alpha = \alpha + \Delta\alpha$;
 end
end

throughout the training process. The dropout probability, α , is increased gradually from 0 to 1 with a step size of $\Delta\alpha$, which determines the number of epochs needed for the LSTM weight sparsity to reach the target sparsity γ . This training method guarantees that the network reaches the target sparsity and the same number of nonzero elements between columns or between subcolumns at the end of the training.

C. Column-Balanced Compressed Sparse Column Format

To fully utilize weight sparsity in an RNN pruned by CBTD, we propose a new sparse weight matrix format method called CBCSC based on the original Compressed Sparse Column (CSC) format [27]. A sparse matrix encoded in CSC has 3 vectors: VAL for nonzero weight elements, index (IDX) containing the indices of elements in VAL, and column pointer

Algorithm 3: CBCSC Format Encoding

Data: \mathbf{A} , a matrix;
 Q , the number of columns in \mathbf{A} ;
 H , the height of columns in \mathbf{A} ;
 M , the number of PEs in a MAC array;
 γ , target sparsity;
Result: Sparse matrix in CBCSC format stored in Value (VAL), local index (LIDX), Burst Length (BLEN);

Build set C containing all columns of \mathbf{A} , where
 $C = \{\mathbf{c}_j | \mathbf{c}_j \in \mathbb{R}^H, 1 \leq j \leq Q, j \in \mathbb{N}\}$;
Shuffle and split columns in set C into subcolumns
 $S\{\mathbf{s}_{ij} | \mathbf{s}_{ij} \in \mathbb{R}^{H/M}, 1 \leq i \leq M, 1 \leq j \leq Q, i, j \in \mathbb{N}\}$;
for $j = 1$ **to** Q **do**
 for $i = 1$ **to** M **do**
 for $k = 1$ **to** H/M **do**
 if $s_{ij}[k] \neq 0$ **then**
 VAL.append($s_{ij}[k]$);
 LIDX.append(k);
 end
 end
 end
end
BLEN = $\lceil H/M * (1 - \gamma) \rceil$;

(CP) containing pointers to the start of a new column. The problem of CSC is that the nonzero elements are not arranged in a regular form that benefits PE access. During run-time, the number of weight elements for each PE at the memory interface is different, requiring arbitration between PEs to ensure the correct dispatching of weights. Arbitration reduces the effective memory bandwidth for weight access. To overcome this problem, we propose CBCSC to force the same number of weight elements for each PE at the memory interface. The procedure of CBCSC encoding is illustrated in Fig. 3 and the steps are described below.

- 1) Assign interleaved rows to PEs. Columns of the weight matrix are sliced, and interleaved elements in each column are grouped into subcolumns. Each subcolumn is assigned to a single PE.
- 2) Find the local index of each nonzero element within the subcolumn it resides in. Zero elements in each subcolumn are discarded, and nonzero elements are aggregated into a dense vector.
- 3) Encode CBCSC by allocating nonzero values and corresponding indices into two vectors VAL, LIDX. Another scalar value called BLEN indicates the number of nonzero elements in each subcolumn. This process is described in Algorithm 3.

In contrast to CSC, the weight matrix encoded by CBCSC has the same number of nonzero elements in VAL for each PE; thus, arbitration is not needed when fetching weight data and the logic area can be reduced.

IV. ACCELERATOR DESIGN

A. Top-level Architecture

Fig. 4 shows the top-level architecture of the Spartus accelerator. The accelerator was implemented on the Programmable Logic (PL) of Xilinx Zynq System-on-a-Chip (SoC), which also has an ARM Cortex-A9 CPU as the host on the Processing System (PS) side. Spartus is composed of a Controller (CTRL), an State Memory (SMEM) block, an Input Processing Unit (IPU), MAC arrays, Weight Memory (WMEM) banks, Adder Treess (AT), and an Output Buffer (OBUF). An Xilinx Direct Memory Access (DMA) IP block controlled by the host is used to manage I/O communications between the accelerator and the host. Input vectors, \mathbf{x}_t , are streamed from PS to PL through the DMA module and buffered in the SMEM block to hide the transfer latency. The SMEM block is also used to buffer LSTM activations \mathbf{h}_t . The IPU concatenates \mathbf{x}_t and \mathbf{h}_t to compute the delta state vectors Δs_t . The delta state vectors are encoded into Nonzero Values (NZV) and Nonzero Indexs (NZI). NZIs are dispatched to CTRL to generate the physical memory addresses of weights in each WMEM bank, and NZVs are dispatched to MAC arrays to be multiplied with the fetched weights. There are N MAC arrays. Each of the first $N - 1$ arrays contains M PEs that perform MxV between NZVs and corresponding weight columns. The last array has M Heterogeneous Processing Elements (HPE) that are also responsible for post-MxV activation generation. The OBUF helps to hide the latency of transferring the last layer's activations to the host.

B. Input Processing Unit (IPU)

The IPU computes delta state vectors Δs_t from both input vectors \mathbf{x}_t and hidden layer activations \mathbf{h}_t . It then generates NZV and NZI that respectively contain the nonzero values of Δs_t and their corresponding indices. As shown in Fig 5, inputs of the IPU are streamed in from the SMEM block. In SMEM, the lengths of \mathbf{x}_t and \mathbf{h}_t vectors are zero-padded to the length that is a multiple of M and concatenated into a single state vector s_t . During the inference, the IPU receives M elements of s_t per clock cycle whenever the state First-In First-Out (FIFO) (S-FIFO) is not full. The state vector $s_t[M - 1 : 0]$ is then partitioned into N equal segments $s_t[M/N - 1 : 0]$, each of which is fed into a DPE shown in Fig. 6. Details of the state vector partition will be discussed in Section V-E.

C. Delta Processing Unit (DPE)

Fig. 6 shows the architecture of the DPE. Following (4)~(7), the DPE calculates a delta vector Δs_t from s_t and s_{t-1} . Each DPE receives a partitioned s_t segment of length $I = M/N$, given that M must be divisible by N . The input elements of a DPE are denoted as $S = \{s_t[i] | 0 \leq i \leq I - 1, i \in \mathbb{N}\}$. s_t is buffered in the IPU input FIFO and s_{t-1} is stored in the look-up table-based memory (Look-up Table based Random Access Memory (LUTRAM)) blocks in the DPE. Each LUTRAM block is addressed by a counter (CNT), which is incremented by one when *valid* is asserted. (4) and (6) are implemented as the Threshold Function (TF) block while (5)

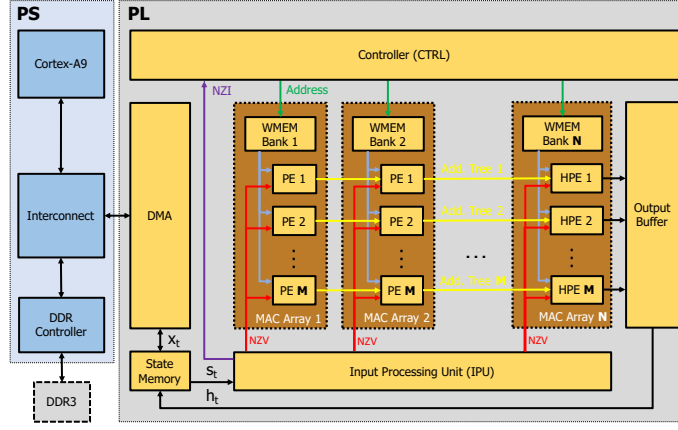


Fig. 4: Spartus accelerator with reconfigurable N MAC arrays, and M PEs in each array.

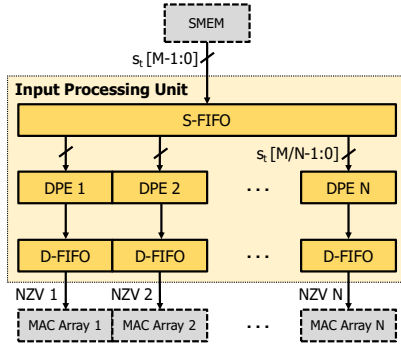


Fig. 5: Structure of the IPU

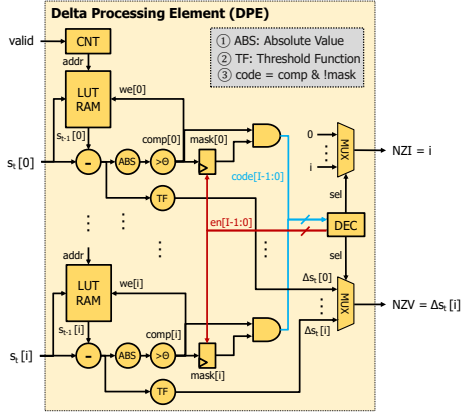


Fig. 6: Simplified data flow of a Delta Processing Element (DPE)

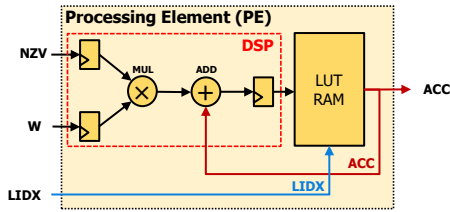


Fig. 7: Architecture of a PE

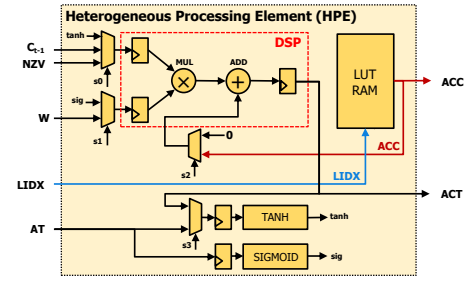


Fig. 8: Architecture of a HPE

and (7) are realized by controlling the write enable ($we[i]$) signal of the LUTRAM using the output of a comparator that produces a high logic state when $|\Delta s_t|$ is larger than the delta threshold Θ . Next, the first nonzero element in Δs_t with its index i are selected as NZV and NZI respectively, by two multiplexers controlled by a Decoder (DEC) according to signal $code[M/N-1:0]$. $code = comp \& mask$, where elements of $mask$ are initialized as ones. Controlled by the signal $en[i]$, when $mask[i] == 1$ and $comp[i] == 1$ in the current cycle, $mask[i]$ is overridden by zero in the next clock cycle. In this way, $mask$ is used to disable nonzero Δs_t once it is already selected and added to the NZV. The NZVs and NZIs generated from DPEs are buffered in their corresponding delta state FIFO (D-FIFO), which drives the input of PEs or HPEs in MAC arrays.

D. Multiply-Accumulate (MAC) Arrays

Sparse Matrix-Sparse Vector Multiplication (SPMxSPV) in Spartus are handled by the N MAC arrays. Each array receives NZVs from its corresponding DPE in the IPU. In Fig. 4, the leftmost $N - 1$ MAC arrays have M PEs and the rightmost MAC array has M HPEs. As shown in Fig. 7, a PE has a MAC unit synthesized by a Digital Signal Processing (DSP) block that performs up to 16-bit by 16-bit multiplication and 48-bit accumulation between NZVs and weights. In addition to the DSP block, the HPE shown in Fig. 8 has multiplexers before each input operand of the DSP to reuse for point-wise multiplication and addition. Furthermore, the HPE also has $tanh$ and $sigmoid$ blocks implemented by look-up tables.

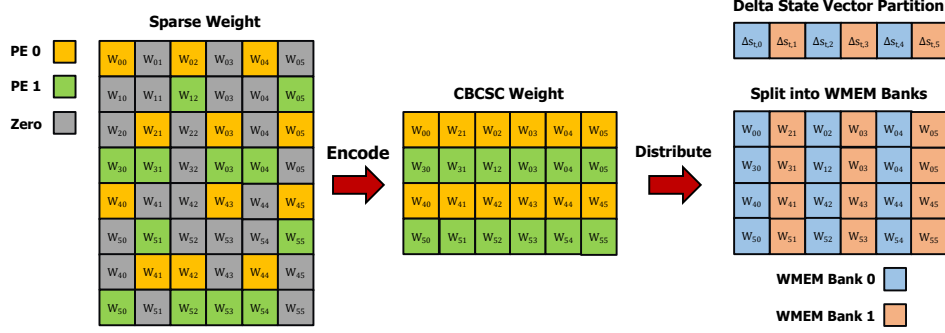


Fig. 9: Sparse DeltaLSTM weights are encoded into CBCSC format and then split into WMEM banks for each MAC array to access independently. We show an example with $N = 2$ MAC arrays and $M = 2$ PEs/HPEs per array.

Each PE or HPE has a dedicated LUTRAM block to buffer their corresponding partial sums. The LUTRAM is addressed by the IDX of weights encoded in the CBCSC format.

After SpMxSpV, delta memory terms DM , defined in (3), are obtained by accumulating partial sums of all MAC arrays by M adder trees. Outputs of the adder trees are then fed to HPEs through the port AT for activation generation. Activation h_t are first stored in SMEM for delta state vector computation of the next time step and then streamed out to the host through DMA.

E. Network Adaptation

The Spartus accelerator supports fixed-point weights and activations. To run a DeltaLSTM network on Spartus, the network should be trained starting with floating-point parameters and quantized to fixed-point numbers before inference. To run an LSTM network with Spartus, weight matrices W_{ii} , W_{hi} , W_{if} , W_{hf} , W_{ig} , W_{hg} , W_{io} , W_{ho} are stacked to a single matrix W_s given by (8).

$$W_s = \begin{pmatrix} W_{ii} & W_{hi} \\ W_{ig} & W_{hg} \\ W_{if} & W_{hf} \\ W_{io} & W_{ho} \end{pmatrix} \quad (8)$$

During matrix-vector multiplication, the stacked weight matrix is multiplied by the delta state vector Δs_t , which follows the same partition pattern as the state vector s_t . Accordingly, W_s is partitioned into N submatrices. Each submatrix only contains columns that will be multiplied by NZVs from its corresponding DPE and are encoded into the CBCSC format, as shown in Fig. 9 and discussed in Section III-C. Then, the interleaved columns of the CBCSC weight are split into N submatrices. Each submatrix is stored in a WMEM bank dedicated to its corresponding MAC array to avoid bank conflict. The delta vector partition follows how the stacked weight matrix is split. The network weights are quantized to 8 bits, while 8 and 10-bit LIDX are used for Spartus and Edge-Spartus, respectively, in the CBCSC format.

V. EXPERIMENTAL SETUP

A. Hardware Implementation

To demonstrate the scalability of Spartus, we evaluated its hardware performance on two configurations with different

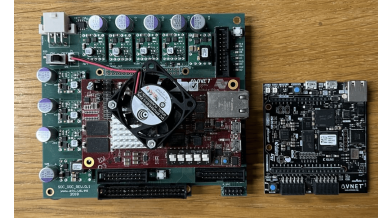


Fig. 10: FPGA development boards used in this work. (Left) AVNET Zynq XC7Z100 with a custom baseboard for Spartus; (Right) AVNET MiniZed XC7Z007S for Edge-Spartus. See Table I.

numbers of PEs, **Spartus** and **Edge-Spartus**, both of which are synthesized in Vivado 2018.2. Spartus is implemented on an AVNET Zynq Mini-Module-Plus (MMP) System-on-Module (SOM) that has a Xilinx Zynq XC7Z100 SoC, the largest Zynq SoC on the market. Edge-Spartus is implemented on an AVNET MiniZed development board having a Zynq XC7007S SoC, the smallest Zynq SoC on the market. Photos of the boards are shown in Fig. 10. Both SoCs have an ARM Cortex-A9 Central Processing Unit (CPU) in their PS as the host. Table I compares the amount of available logic and memory resources and the cost of both Zynq SoCs with those used by other RNN accelerators.

The Spartus accelerator resides on the PL side of both SoCs and is controlled by bare-metal C programs compiled in the Xilinx Software Development kit (SDK). The Spartus accelerator buffers network weights using on-chip Block Random Access Memory (BRAM) and the C program initializes LSTM weights in the DDR3 Dynamic Random Access Memory (DRAM) and then streams weights to the on-chip WMEM banks synthesized with BRAMs. In Edge-Spartus, the on-chip BRAM capacity is too small to buffer the large network; thus the program initializes weights in off-chip DDR3L DRAM and the accelerator fetches weights from the High Performance (HP) AXI4 slave port interfacing PL and PS.

B. Feature Extraction & Network Setup

We evaluate the impact on the accuracy of both the CBTD method and DeltaLSTM algorithm on a speech recognition task using the TIMIT and larger Librispeech datasets.

TABLE I: Comparison of FPGA chips ordered according to their on-chip memory size in Megabits (Mb).

FPGA	DSP	¹ BRAM/M20K	² LUT/ALM	FF	Process	³ Cost	RNN Accelerator
XC7Z007S	66	50 (1.8 Mb)	14,400	28,800	28nm	\$55	EdgeDRNN [23], Edge-Spartus
XC7Z100	2,020	755 (26.5 Mb)	277,400	554,800	28nm	\$3,192	DeltaRNN [22], Spartus
XCKU060	2,760	1,080 (38.9 Mb)	331,680	663,360	20nm	\$3,978	Efficient Speech Recognition Engine (ESE) [12]
SX660	3,376	2,133 (41.7 Mb)	250,540	1,002,160	20nm	N/A	E-LSTM [16]
XC7VX690T	3,600	1,470 (51.7 Mb)	433,200	866,400	28nm	\$17,926	C-LSTM [19], E-RNN [20]
GX1150	3,036	2,713 (53.0 Mb)	427,200	1,708,800	20nm	N/A	BBS [15]

¹ Single BRAM Size = 36 Kb. Single M20K size = 20 Kb.

² The look-up table (LUT) in Xilinx FPGAs [28] is not equivalent to the Adaptive Logic Module (ALM) in Intel FPGAs [29].

³ Costs extracted from Digi-Key US in March 2022.

The TIMIT dataset [30] has a standard 462 speaker training set with all dialect sentences (SA) removed following [4]. The development (DEV) and test (TEST) sets have utterances of 50 and 24 speakers respectively. 123-dimensional features are extracted from the input and consist of the 40 coefficients of FFT-based filter banks distributed on a Mel-scale, plus the energy term; and their first and second-order temporal derivatives [4]. The Connectionist Temporal Classification (CTC) loss function [31] is used during training so that the final logit layer of the acoustic model (AM) generates phonemes directly without requiring a sophisticated decoding algorithm. The Phone Error Rate (PER) results were collected using a simple greedy decoder that selects the index of the phoneme class with the highest score.

The large-scale LibriSpeech dataset has 1000 hours of audiobook speech based on LibriVox’s library [32]. For Librispeech, we followed the same AM training process leading to the LSTM baseline in the PyTorch-Kaldi framework using the 100-hour subset [33]. We used the Kaldi toolkit [34] to extract 40-dimensional feature-space maximum likelihood linear regression (fMLLR) features [35] and decode the AM output using a Viterbi decoder with a 4-gram language model to calculate the Word Error Rate (WER). The PyTorch-Kaldi [33] framework was used to train the AM. We used this training and evaluation process to have a fair comparison with the PyTorch-Kaldi baseline and the HCGS [17] method.

We trained LSTM-AMs on both datasets. The last LSTM layer is followed by a Fully-Connected Layer (FCL) having the same number of units and a final logit layer. The networks implemented on the Spartus hardware accelerators are quantized during training to 8-bit weights and 16-bit activations using the dual-copy rounding method [36].

C. Pretrain & Retrain

We adopted a pretrain-retrain process for this task to train networks with spatio-temporal sparsity. For the TIMIT dataset, during the pretrain phase, the LSTM layers were initialized and trained with the CBTD applied for 150 epochs. We set the step size of dropout probability $\Delta\alpha$ to 1/30 so that the target sparsity γ was achieved within the first 30 epochs and maintained during the remaining epochs. For the Librispeech dataset, we pretrain the networks for 24 epochs (the same as the PyTorch Kaldi baseline) and anneal the step size of dropout probability of CBTD during the first 10 epochs. The CBTD was also applied to the FCL with the same $\Delta\alpha$ and γ . The pretraining process was early stopped at the epoch that achieved the best accuracy on the development set.

During the retraining phase, weights of the pretrained LSTM layers are copied into DeltaLSTM layers of the same size to be retrained for 50 epochs for the TIMIT dataset and 5 epochs for the Librispeech dataset with $\alpha = 1$. The retrain phase was also early stopped at the best accuracy on the development set. The final accuracy results for the TIMIT dataset are reported on the core test set, which has 192 samples. For Librispeech, the final WER results were evaluated on the standard test set.

VI. RESULTS

A. Design Space Exploration

We determine how the number of PEs, and MAC arrays; and the delta threshold Θ , impact the accuracy and hardware performance as evaluated on TIMIT.

1) *Pretrain: Phone Error Rate vs. Weight Sparsity*: This section reports the impact of CBTD on weight sparsity and accuracy. Fig. 11(a) & Fig. 11(b) show the evolution of PER on the development set (DEV-PER) over the target sparsity. Each data point in Fig. 11 is the average value over 5 runs. We explored using different numbers M of PEs per MAC array, with values of $M=32/64/128$ for the CBTD method. The horizontal dashed line shows the DEV-PER of the network with 32-bit floating-point (FP32) parameters trained without using CBTD and quantization, which achieved 20.30% DEV-PER.

Results show that the accuracy with different numbers of PEs is similar. Most of the DEV-PER values of LSTM networks trained with CBTD were worse than the FP32 baseline when the target sparsity is below 40%. Similar to the Dropout [37] and Targeted Dropout [13] regularization methods, CBTD helped regularize the LSTM network. Target sparsity γ between 50% and 90% resulted in better DEV-PER than FP32 due to the regularization effect of CBTD. A similar regularization effect on the TIMIT dataset due to weight pruning on LSTM was also observed in [15]. The best PER results are achieved when γ is between 90% and 94%. The pretrained networks with CBTD achieve up to 96% weight sparsity without loss of accuracy when compared to the FP32 baseline results. To achieve the best PER while having speedup as high as possible, the network having 94% weights sparsity was used in the retrain phase, which achieves a DEV-PER value of around 19.30% among the best PER values of all sparsity levels.

2) *Retrain: Phone Error Rate vs. Delta Threshold*: The purpose of the retrain phase is to induce temporal sparsity using the DeltaLSTM model. Temporal sparsity introduces

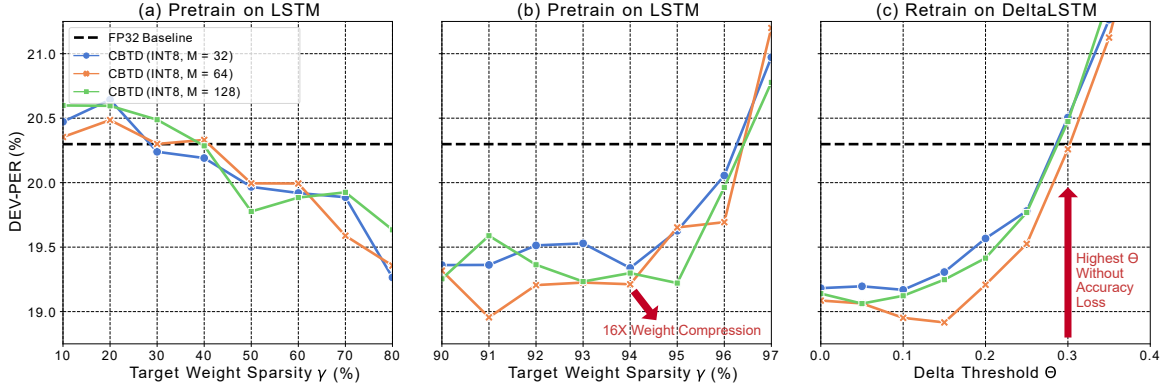


Fig. 11: PER evaluated on the TIMIT development set (DEV-PER). (a) and (b) show the dependence of PER on different target weight sparsity values after the 150-epoch pretrain phase on LSTM. (a) PER from $\gamma = 10\%$ to $\gamma = 80\%$ (step size = 10%). (b) PER from $\gamma = 90\%$ to $\gamma = 97\%$ (step size = 1%). (c) PER after the 50-epoch retrain phase on DeltaLSTM for different delta thresholds. The pretrained models with $\gamma = 94\%$ from (b) were used in the retrain phase. Results were averaged from 5 runs.

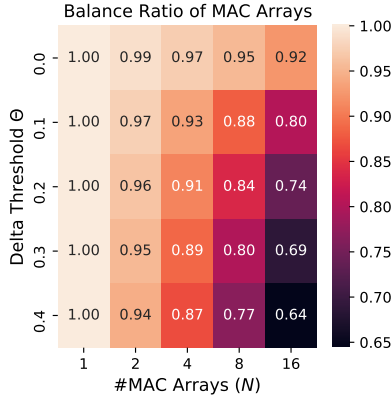


Fig. 12: Balance ratio of MAC arrays with respect to delta threshold and the number of MAC arrays in the Spartus accelerator. The values were obtained by running the hardware over all TIMIT core test set samples.

zero elements that can be skipped to save the computations and the memory access but can lead to accuracy degradation once the sparsity is higher than a certain value. This section reports the results of the retrain phase and explores the optimal condition to achieve a balance between speedup and accuracy.

Fig. 11(c) shows the DEV-PER of the network retrained with DeltaLSTM layers. During the retraining phase, various delta thresholds Θ were used. The same thresholds were applied to all LSTM layers. The CBTD was still used during the whole training phase with a step size of dropout rate α fixed to 1. Results show that DEV-PER increases with increased delta thresholds Θ and the network trained with $M = 64$ achieves the best DEV-PER which is lower than the FP32 baseline until $\Theta > 0.3$. Thus, we set $\Theta = 0.3$ to evaluate the performance of the accelerator in Sec. VI.

3) *Workload Balance Between MAC Arrays*: The theoretical peak throughput ν_{Peak} of the accelerator on the PL is given as:

$$\nu_{Peak} = 2 \cdot f_{pl} \cdot K \quad (9)$$

where f_{pl} is the operation clock frequency of the PL and K is the total number of MAC units. In Spartus, $K = M \times N$, where N is the number of MAC arrays. Thus, the theoretical peak throughput is proportional to the number of MAC arrays; however, the actual hardware throughput is affected by the workload imbalance between MAC arrays.

Unlike the structured sparse weight matrix induced by CBTD, the sparsity pattern of the delta state vector s_t is dynamically updated during LSTM inference in each time step. Therefore, partitioned Δs_t vector segments, which are encoded as NZVs by DPEs, are likely to have different numbers of nonzero values in each time step of the LSTM computation. Provided that there are N MAC arrays in the accelerator, the workload (WL), which is the number of nonzero elements of Δs_t allocated to the n -th MAC array at time step t , is \mathbf{WL}_t^n . Then, the Balance Ratio (BR) of MAC arrays is given as:

$$\begin{aligned} \mathbf{BR} &= \frac{\sum_{t=1}^T \mathbf{WL}_{t,mean}}{\sum_{t=1}^T \mathbf{WL}_{t,max}} \\ \mathbf{WL}_{t,mean} &= \frac{\sum_{n=1}^N \mathbf{WL}_t^n}{N} \\ \mathbf{WL}_{t,max} &= \max(\mathbf{WL}_t^1, \mathbf{WL}_t^2, \dots, \mathbf{WL}_t^N) \end{aligned} \quad (10)$$

where $\mathbf{WL}_{t,mean}$ and $\mathbf{WL}_{t,max}$ are respectively the mean and max workload of all MAC arrays at time step t . The BR is obtained by running the hardware on a temporal sequence with a length of T and getting the sum of $\mathbf{WL}_{t,mean}$ and $\mathbf{WL}_{t,max}$ over T time steps. The performance of hardware is bottlenecked by the max workload $\mathbf{WL}_{t,max}$ at each time t . The optimal workload balance can be achieved once the workload of each MAC array equals to $\mathbf{WL}_{t,mean}$. Therefore, the closer BR is to 1, the more balanced the workload between MAC arrays.

Fig. 12 shows the BR values of MAC arrays evaluated on all samples in the core test set of TIMIT running the best DeltaLSTM network selected after the retraining phase. Increasing delta threshold Θ or the number of PEs resulted in a more imbalanced allocation of nonzero elements be-

TABLE II: Accuracy results on the core test set of TIMIT with different sizes of LSTM networks and optimization methods. (**L** denotes the number of LSTM layers; **H** denotes the number of units in each LSTM layer; **UNI** denotes that the network is unidirectional; the bold network names are supported by Spartus, and the bold rows have the highest arithmetic operations saving without losing accuracy; results were averaged from 5 runs.)

Network	γ	Θ	Weight Precision	Model Size (MB)	Weight Sparsity (%)	Temporal Sparsity (%)	TEST-PER (%)	Accuracy Improvement (%)	Arithmetic Operations Saving
LSTM-3L-512H-UNI	-	-	FP32	23.18	0	0	22.7±0.16	0	1×
	-	-	INT8	5.79	0	0	22.8±0.50	-0.1	1×
LSTM-3L-512H-UNI-CBTD (w/ Spatial Sparsity)	0.80	-	INT8	1.27	78.13	0	21.5±0.12	1.3	4.6×
	0.90	-	INT8	0.72	87.50	0	21.3±0.54	1.4	8.0×
	0.94	-	INT8	0.36	93.75	0	22.6±0.47	0.2	16.0×
	0.97	-	INT8	0.18	96.88	0	25.7±0.56	-2.9	32.1×
LSTM-2L-768H-UNI	-	-	FP32	30.88	0	0	23.2±0.36	0	1×
	-	-	INT8	8.10	0	0	23.4±0.31	0.2	1×
LSTM-2L-768H-UNI-CBTD (w/ Spatial Sparsity)	0.80	-	INT8	1.69	79.17	0	21.7±0.27	1.5	4.8×
	0.90	-	INT8	0.84	89.58	0	21.4±0.15	2.0	9.6×
	0.94	-	INT8	0.51	93.75	0	22.4±0.96	0.8	16.0×
	0.97	-	INT8	0.34	95.83	0	22.5±0.32	0.7	24.0×
LSTM-2L-1024H-UNI	-	-	FP32	56.81	0	0	22.3±0.29	0	1×
	-	-	INT8	14.20	0	0	22.0±0.29	0.3	1×
LSTM-2L-1024H-UNI-CBTD (w/ Spatial Sparsity)	0.80	-	INT8	2.88	79.69	0	21.1±0.31	0.9	4.9×
	0.90	-	INT8	1.55	89.06	0	20.8±0.33	1.5	9.1×
	0.94	-	INT8	0.89	93.75	0	20.6±0.27	1.7	16.0×
	0.97	-	INT8	0.44	96.88	0	22.7±0.39	-0.4	32.1×
DeltaLSTM-2L-1024H-UNI-CBTD (w/ Spatio-Temporal Sparsity)	0.94	0.1	INT8	0.89	93.75	74.22	20.6±0.30	1.7	62.1×
	0.94	0.3	INT8	0.89	93.75	90.60	21.8±0.30	0.6	170.2×

TABLE III: Accuracy results on the test set of Librispeech with different sizes of LSTM networks and optimization methods trained on the 100-hour training set. (**BI** denotes that the network is bidirectional; Accuracy Improvement is the WER difference to the baseline floating-point conventional RNN.)

Network	γ	Θ	Weight Precision	Model Size (MB)	Weight Sparsity (%)	Temporal Sparsity (%)	TEST-WER (%)	Accuracy Improvement (%)	Arithmetic Operations Saving
LSTM-4L-512H-BI (PyTorch-Kaldi Baseline [33])	-	-	FP32	14.84	0	0	6.4	-	1×
LSTM-4L-512H-BI-CBTD (w/ Spatial Sparsity)	0.90	-	INT8	0.46	87.5	0	6.2	0.2	8.0×
	0.94	-	INT8	0.23	93.75	0	7.1	-0.7	16.0×
LSTM-3L-512H-UNI	-	-	FP32	21.3	0	0	7.0	-	1×
LSTM-3L-512H-UNI-HCGS [17] (w/ Spatial Sparsity)	-	-	INT6	0.29	93.75	0	11.4	-4.4	16.0×
LSTM-3L-512H-UNI-CBTD (w/ Spatial Sparsity)	0.94	-	INT8	0.33	93.75	0	7.3	-0.3	16.0×
LSTM-2L-1024H-UNI	-	-	FP32	56.81	0	0	8.0	-	1×
	-	-	INT8	14.20	0	0	7.6	0.4	1×
LSTM-2L-1024H-UNI-CBTD (w/ Spatial Sparsity)	0.80	-	INT8	2.88	79.69	0	6.7	1.3	4.9×
	0.90	-	INT8	1.55	89.06	0	6.5	1.5	9.1×
	0.94	-	INT8	0.89	93.75	0	7.0	1.0	16.0×
	0.97	-	INT8	0.44	96.88	0	8.3	-0.3	32.1×
DeltaLSTM-2L-1024H-UNI-CBTD (w/ Spatio-Temporal Sparsity)	0.94	0.05	INT8	0.89	93.75	80.45	7.4	0.6	81.8×
	0.94	0.1	INT8	0.89	93.75	89.91	8.5	-0.5	158.6×

tween MAC arrays. To maximize the hardware performance at $\Theta = 0.3$, we set the number of MAC arrays between $N = 8$ and $N = 16$, where BR is between 0.8 and 0.69. Thus, the loss of hardware performance due to workload imbalance is 20% to 31%, which is small compared to the $8\times$ to $16\times$ peak throughput gain by increasing N from 1 to 8 and 16. However, using $N > 8$ resulted in routing congestion. FPGA Therefore, we set $M = 64$ MAC arrays and $N = 8$ PEs for our final Spartus implementation. For Edge-Spartus, we set $M = 4$ and $N = 1$ to have a similar off-chip DRAM bandwidth as the EdgeDRNN accelerator (EdgeDRNN requires 64 bits per clock cycle while Edge-Spartus requires 72 bits per clock cycle) for a relatively fair comparison in Sections VII-A and VII-B.

B. Model Accuracy

We evaluated the final accuracy of our AM using our proposed training and optimization methods on the TIMIT and Librispeech test sets with $M = 64$ and different delta thresholds.

1) *TIMIT*: To demonstrate the effectiveness of CBTD, we trained the AMs with various numbers of layers and layer sizes on the TIMIT dataset, as shown in Table II. The largest network has two unidirectional LSTM layers with 1024 units per layer, which is the same as the networks used in ESE [12] and other related previous works, including C-LSTM [19], E-RNN [20], BBS [15] and E-LSTM [16]. We observe that networks pretrained with our CBTD method result in better PER on the test set than the corresponding FP32 baselines when the spatial (weight) sparsity is roughly between 80% and 94%. Networks are likely to have worse PER when the spatial

sparsity is $\geq 97\%$. These results on the TIMIT test set are consistent with those shown in Fig 11 on the development set. In short, our CBTD method achieves $16\times$ lossless compression of the various sizes of AMs. The previous works either could not achieve the same level of model compression rate or had worse accuracy loss. By further adding temporal sparsity on top of spatial sparsity, our spatio-temporal DeltaLSTM network achieves $170\times$ saving of arithmetic operations and memory access of the $M\times V$ in the LSTM layers, which is significantly better than previous works. Fig. 13(a) shows the impact of different delta threshold values on the temporal sparsity evaluated on the TIMIT core test set, and the values are the average temporal sparsity over the 2 DeltaLSTM layers. Overall, the sparsity of delta input state vector Δx is lower than delta hidden state vector Δh . This is due to the small temporal sparsity in the input layer of the whole network to allow enough input stimuli to be fed into the network. The delta hidden states can be up to 90% sparse when the threshold is larger than 0.3. Fig. 13(b) shows the PER on the core test set (TEST-PER) versus the delta threshold. The FP32 baseline on the test set was 22.30%. Similar to DEV-PER results, the DeltaLSTM network achieves better TEST-PER when the delta threshold Θ is smaller than 0.3. With small delta thresholds, the DeltaLSTM shows a slight regularization effect that helped to achieve the best TEST-PER at 20.63%. With $\Theta = 0.3$, the TEST-PER is 21.75% which corresponds to 0.55% accuracy improvement compared to the FP32 baseline.

2) *Librispeech*: Beyond the simpler TIMIT dataset, we also evaluate the effectiveness of cost saving and accuracy impact of our methods on the large-scale corpus, Librispeech, which has not been evaluated in previous FPGA RNN accelerators. Results are shown in Table III. We first applied CBTD on the bidirectional LSTM used in the PyTorch-Kaldi baseline [33] and obtained $8\times$ arithmetic operations saving with 0.2% better WER than the baseline. $16\times$ saving is achievable with 0.7% accuracy loss. The bidirectional LSTM networks achieve the highest accuracy but are not usable in real-time speech recognition systems because they must receive the whole sentence to recognize a single frame. Thus, we are more interested in evaluating our methods on unidirectional LSTM networks. To our knowledge, HCGS [17] is the only previous structured pruning method evaluated on Librispeech. However, the sparse weight pattern of HCGS is predefined at the network initialization stage and maintained throughout training with only changeable weight magnitudes, greatly limiting its ability to find subnets with good accuracy, as discussed in *The Lottery Ticket Hypothesis* [38], [39]. CBTD allows both removal and addition of connections during training with only constraints on the distribution of nonzero values across predefined submatrices, which could lead to higher accuracy with the same level of model compression. We applied CBTD on a unidirectional LSTM network of the same size as reported in [17]. With the same $16\times$ saving in arithmetic operations, CBTD has only 0.3% higher WER while HCGS caused $10\times$ higher accuracy loss. Finally, we applied our methods to the AM model used for hardware evaluation. We found that the combination of INT8 quantization, CBTD, DeltaLSTM achieves $64\times$ model compression and $81.8\times$ arithmetic operations saving compared

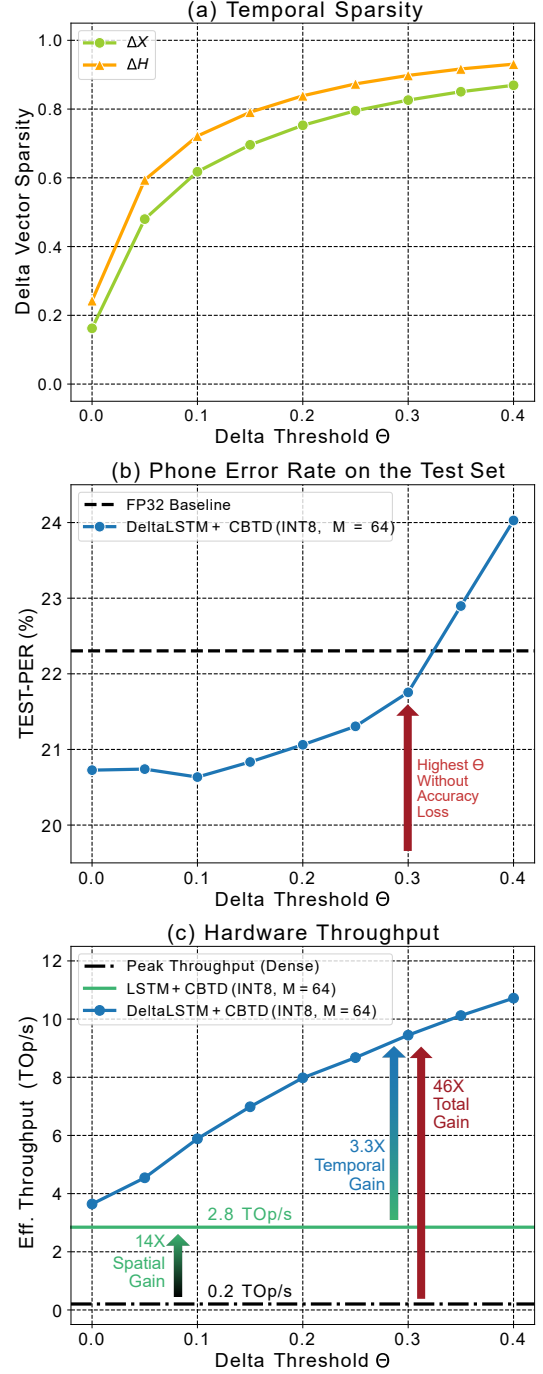


Fig. 13: (a) shows the temporal sparsity of the DeltaLSTM-2L-1024H-UNI-CBTD network. Δx and Δh are respectively the delta input and delta hidden vectors; (b) shows the PER of the DeltaLSTM network evaluated on the core test set of TIMIT; (c) shows the batch-1 throughput of the Spartus accelerator versus delta thresholds. The theoretical peak throughput is computed using (9).

to the corresponding FP32 baseline. Another important observation is that networks pruned by CBTD during training with conservative pruning rates (less or equal to 94% for TIMIT and 90% for Librispeech) all led to better accuracy, proving that CBTD well preserves the regularization effect of pruning,

TABLE IV: Performance summary of Spartus and Edge-Spartus with progressive levels of optimizations (Sec. VI-C)

	Settings	Batch-1 Eff. Throughput (GOp/s)		Latency (μ s)	
		Spartus	Edge	Spartus	Edge
No Opt.	-	<204.8	<1.0	>46.0	>9420.8
+CBTD	$\gamma = 0.94$	2845.4	17.7	3.3	530.2
+DeltaLSTM	$\Theta = 0.1$	5885.0	34.8	1.6	270.6
	$\Theta = 0.3$	9447.8	77.3	1.0	121.7

as suggested by related works [38]–[40].

C. Hardware Performance: Throughput & Latency

Since we focus on achieving low latency LSTM inference, in this work, we evaluate the hardware performance with a batch size of 1. The test network is the top layer of our biggest AM having 1024 hidden units, which is the same as previous state-of-the-art FPGA RNN accelerators [12], [15], [16], [19], [20].

Table IV summarized the performance of Spartus and Edge-Spartus with progressive levels of optimizations. With $M \times N = 512$ MAC units, the theoretical baseline performance of Spartus is only 0.2 TOP/s, calculated using (9). With the highest level of optimization, Spartus can finish the inference of the big DeltaLSTM layer within 1 μ s, corresponding to 9.4 TOP/s effective throughput and 46 \times speedup versus the baseline. Fig. 13(c) further shows how much the spatial and temporal sparsity contributes to the total speedup. By applying only CBTD to the LSTM network to induce 94% spatio sparsity (16 \times pruning rate), the Spartus achieves 2.8 TOP/s batch-1 throughput, corresponding to a 14X spatial gain the baseline. After retraining the sparse LSTM layers as DeltaLSTM, further speedup was achieved. With a zero delta threshold, the accelerator achieves 3.6 TOP/s batch-1 throughput. By increasing the delta threshold to 0.3, which is the highest value with better TEST-PER over FP32 baseline on TIMIT, Spartus achieves 9.4 TOP/s batch-1 throughput, which is another 3.3 \times temporal gain on top of spatial gain. Overall, by combining the 14 \times spatial gain and 3.3 \times temporal gain, Spartus achieves 46 \times speedup by exploiting spatio-temporal sparsity.

Table IV also reports the performance of Edge-Spartus, which was implemented on the FPGA of the smallest Zynq SoC, which has only 0.2 MB on-chip memory and cannot buffer the networks on-chip even after compression. By relying solely on off-chip DDR3L memory bandwidth to fetch the network weights, Edge-Spartus achieves 121.7 μ s latency, which is still orders of magnitude faster than the normal 10 ms frame shift used in real-time speech recognition systems [3], [41]

VII. DISCUSSION

A. Comparing Spartus with Previous Works on TIMIT

FPGA ESE was the first RNN accelerator that adopted weight pruning to speedup LSTM inference. However, ESE was designed for throughput-oriented inference using large batch sizes. Performance of ESE was tested with a batch

size of 32. DeltaRNN exploited temporal sparsity to accelerate GRU RNNs, but the test network was small compared to other works. C-LSTM and E-RNN used a structured weight matrix with an FFT-based computing mechanism to reduce operations during inference. Table V provides the performance of C-LSTM and E-RNN with the 16 \times compression ratio reported in the original papers. E-LSTM and BBS adopted structured pruning methods to achieve finer-grained workload balance compared to ESE, and their performance was evaluated with batch sizes of 8 and 1, respectively. BBS achieved the best batch-1 throughput and latency among all previous RNN accelerators. Since we focus on achieving low-latency LSTM inference, for a fair comparison, we computed the performance of ESE and E-LSTM with a batch size of 1 in Table V. Power numbers of Spartus and other accelerators are measured using the wall-plug power of the FPGA board.

We include 'Latency' and 'Frame per Second (FPS)' to represent the performance of accelerators on their own test networks. Spartus achieves the highest FPS and lowest inference latency among all platforms. However, the test network sizes are different across platforms. Spartus and E-LSTM used test networks with normal LSTM units, while ESE, C-LSTM, E-RNN, and BBS used a Google LSTM network with the same number of neurons but because their neuron model has peephole connections and projection layers that shrink the dimension of both recurrent and output connections [42], leading to an overall decrease in the number of network parameters. Thus, we include 'Effective Throughput' and 'Power Efficiency' metrics which take into the number of total operations for computing these networks in the comparison across these accelerators. Compared to DeltaRNN, which also exploited temporal sparsity, Spartus achieves 8 \times higher effective throughput and 7 \times higher power efficiency. Compared to C-LSTM and E-RNN which achieved the same 16 \times weight compression ratio, Spartus achieves around 10 \times higher FPS and 8 \times lower latency. By exploiting spatio-temporal sparsity, Spartus achieves 4 \times higher batch-1 effective throughput than BBS, which was the state-of-the-art accelerator with the highest batch-1 effective throughput.

Table V also includes the resource utilization and names of the FPGA chips. Table I compares FPGAs. A larger FPGA can buffer larger networks on-chip to provide sufficient memory bandwidth to more physical MAC units. New process technologies can help the same accelerator architecture to achieve higher clock frequencies after implementation. It can be observed that Spartus achieves higher performance than previous accelerators even on a smaller FPGA with the earlier 28nm process, except for DeltaRNN that used the same XC7Z100 FPGA.

B. Comparing Edge-Spartus to EdgeDRNN and ESE

Most previous accelerators achieve their high batch-1 throughput by storing the RNN weights completely on-chip, which is not practical in edge applications using resource-constrained hardware platforms. EdgeDRNN [23] and ESE [12] are the only two previous FPGA RNN accelerators that reported real performance numbers with the off-chip memory bandwidth bottleneck. Thanks to the scalable

TABLE V: Comparison of Spartus with prior state-of-the-art RNN accelerators on FPGA (Batch Size = 1)

	ESE [12]	DeltaRNN [22]	C-LSTM [19]	E-RNN [20]	BBS [15]	E-LSTM [16]	Spartus (Ours)
#Parameters (M)	3.25	0.20	3.25	3.25	3.25	4.82	4.70
Compressed #Parameters (M)	0.36	-	0.20		0.41	0.60	0.29
Bit Precision (Activation/Weight/Index)	INT16/12/4	INT16/16/0	INT6/16/0	INT16/16/0	INT16/16/4	INT8/8/4	INT16/8/8
Weight Sparsity (%)	88.78	0	93.75		87.5		93.75
Act./Temp. Sparsity (%)	0	92.5	0		58		82.56
PER on TIMIT (%)	20.7	-	24.6	20.3	23.6	23.2	21.8±0.3
Language Model?	Yes	-	Unreported			No	No
FPGA Platform	XCKU060	XC7Z100	7V3	XC7VX690T	GX1150	SX660	XC7Z100
DSP (%)	54.5	38.0	74.3	79.6	100	1.4	25.7
BRAM/M20K (%)	87.7	60.6	65.7	65.2	92	32.1	33.0
LUT/ALM (%)	88.6	94.2	58.7	59.4	68	87.8	49.2
FF (%)	68.3	21.5	46.5	55.3	N/A	15.6	19.5
Frequency (MHz)	200	125	200				200
#MACs	32	768	128		4096	128	512
Peak Throughput (GOp/s)	12.8	192	51.2		1638.4	51.2	204.8
Effective Throughput (GOp/s)	78.6	1198.0	714.3	783.1	2432.8	403.3	9447.8
Speedup	6.1×	6.2×	14.0×	15.3×	1.5×	7.9×	46.1×
Latency (us)	82.7	-	9.1	8.3	2.4	23.9	1.0
Frame per Second (kFPS)	12	-	110	120	417	42	1,001
Wall Power (W)	41.0	7.3	23.0	25.0	19.1	15.9	8.4
Wall Power Efficiency (¹ GOp/s/W)	1.9	164.1	31.1	31.3	127.4	25.4	1124.7

¹ GOp/s/W is equivalent to GOp/J.

TABLE VI: Comparison of Edge-Spartus with EdgeDRNN (Batch Size = 1)

	EdgeDRNN [23]	Edge-Spartus (Ours)
#Parameters (M)	5.4	4.7
Compressed #Parameters (M)	-	0.29
Bit Precision (Activation/Weight/Index)	INT16/8/0	INT16/8/10
Weight Sparsity (%)	0	93.75
Act./Temp. Sparsity (%)	90.01	82.56
FPGA Platform	XC7Z007S	
DSP (%)	13.6	7.6
BRAM (%)	66.0	76.0
LUT (%)	65.2	78.5
FF (%)	34.1	41.5
Frequency (MHz)	125	
#MACs	8	4
Latency (us)	536	121.7
Frame per Second (kFPS)	1.9	8.2
Peak Throughput (GOp/s)	2.0	1.0
Effective Throughput (GOp/s)	20.2	77.3
Speedup	10.1×	77.3×
Accelerator Core Power (μ W)	66	69
Core Power Efficiency (GOp/s/W)	306	1120
FPGA On-Chip Power (W)	1.4	
On-Chip Power Efficiency (GOp/s/W)	14.2	53.3
Wall Power (W)	2.3	
Wall Power Efficiency (GOp/s/W)	8.8	33.6

architecture of Spartus, we could fit Edge-Spartus with 4 PEs on the tiny FPGA in the Zynq XC7007S SoC. Edge-Spartus uses INT8 weights with a 10-bit local index for each weight; thus, the off-chip memory interface bit-width is 72-bits; while the previous EdgeDRNN with 8 PEs used INT8 weights and requires a 64-bit off-chip memory interface. With the same DDR3L off-chip memory as EdgeDRNN on the MiniZed board, Edge-Spartus achieves 77.3 GOp/s batch-1 effective throughput, which is around 4× higher than EdgeDRNN and close to that of ESE, which uses 8× more MAC units on an FPGA that costs 70× more.

C. DRAM Power Efficiency

On-chip memory fetch consumes over 10× higher energy than arithmetic operations with the same numbers of bits and can be over 1000× when using off-chip DRAM [9],

TABLE VII: Off-chip DRAM access energy.

DRAM Type	DDR3	DDR3L	GDDR6	HBM2
Access Energy/Bit (pJ)	20.3 [9]	¹ 16.5	5.5 [43]	3.9 [44]

¹ The DDR3L (1.35 V) access energy is estimated by scaling down the number of DDR3 (1.5 V) according to their supply voltages.

[10]. For a memory-bounded algorithm such as LSTM, the key to enhancing power efficiency is to reduce the amount of memory access per inference. Using Edge-Spartus, we analyzed the potential reduction of energy consumption per frame using various types of DRAM (Table VII) and showed the results in Fig. 14. By exploiting spatio-temporal sparsity, the DRAM access energy can be reduced by 91.7×. However, this reduction of energy does not completely translate to the power efficiency of the whole system, of which other peripheral modules can also be an important source of power consumption. For example, our XC7Z100 SOM lacks a usable PS sleep mode and thus consumes 1.8 W even at idle. Thus, although the power efficiency obtained using wall power reflect the real-world performance of different accelerators, they are biased by the boards they are implemented on. Our comparison between EdgeDRNN and Edge-Spartus showcases how much improvement of power efficiency can be achieved on the same platform by exploiting spatio-temporal sparsity, and Edge-Spartus achieves roughly 4× higher core and system power efficiency than EdgeDRNN.

VIII. CONCLUSION

We proposed Spartus, the first LSTM accelerator that exploits spatio-temporal sparsity to enable the lowest latency and the highest power efficiency in RNN inference compared to previous work. The spatial weight sparsity was implemented using our newly proposed structured CBTD pruning method. CBTD achieves a comparable compression rate as previous weight compression methods with negligible accuracy loss. The benefit of CBTD over previous methods is

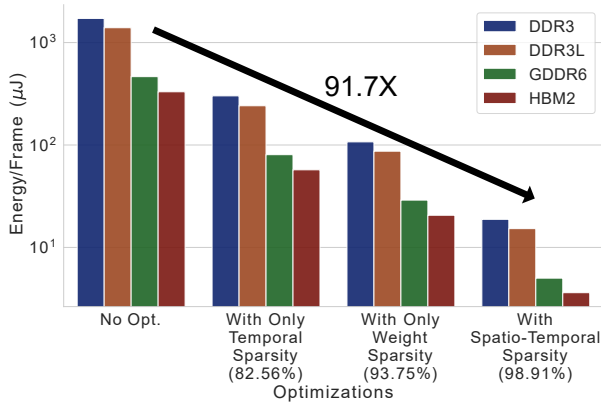


Fig. 14: Estimated Off-chip DRAM access energy of Edge-Spartus per inference (Frame).

the compatibility with the DN algorithm. Temporal sparsity is achieved through the DeltaLSTM model by applying the delta network algorithm to the LSTM model. The Spartus accelerator is implemented on a Xilinx Zynq 7100 FPGA running at 200 MHz. Evaluated on the TIMIT dataset, Spartus achieves 9.4 Top/s effective batch-1 throughput and 1.1 Top/J power efficiency, which is respectively $4\times$ and $7\times$ higher than the previous state-of-the-art. Compared to the theoretical peak hardware performance, which runs a dense LSTM layer with 1024 neurons in $46\mu\text{s}$, Spartus runs the same network in $1\mu\text{s}$ by jointly exploiting structured spatial sparsity ($14\times$ speedup) and temporal sparsity ($3.3\times$ speedup) to achieve $46\times$ speedup in total. For light-weight and low-cost edge applications, Edge-Spartus provides over 75 GOp/s effective throughput for arbitrary-sized LSTM-RNNs on a \$55 USB-powered MiniZed board, which will be useful for edge signal processing and mobile robots. Compared to ASIC-based RNN accelerators [17] which mainly focus on low power processing, Spartus achieves significantly higher effective throughput but also massively more power consumption due to its implementation in FPGAs. A future ASIC implementation of Spartus could achieve even higher power efficiency and throughput than the existing FPGA-based systems.

ACKNOWLEDGMENT

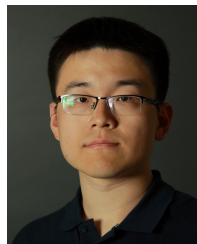
We thank X. Chen and other Sensors Group members for discussion on general design concepts. We thank A. Rios-Navarro, R. Morales, and A. Linares-Barranco from the University of Seville for creating the baseboard for our FPGAs.

REFERENCES

- [1] S. Hochreiter and J. Schmidhuber, "Long short-term memory," *Neural Comput.*, vol. 9, no. 8, pp. 1735–1780, Nov. 1997, ISSN: 0899-7667. DOI: 10.1162/neco.1997.9.8.1735. [Online]. Available: <http://dx.doi.org/10.1162/neco.1997.9.8.1735>.
- [2] K. Cho, B. van Merriënboer, C. Gulcehre, F. Bougares, H. Schwenk, and Y. Bengio, "Learning phrase representations using rnn encoder-decoder for statistical machine translation," in *Conference on Empirical Methods in Natural Language Processing (EMNLP 2014)*, 2014.
- [3] D. Amodei, S. Ananthanarayanan, R. Anubhai, et al., "Deep Speech 2: End-to-end speech recognition in English and Mandarin," in *International conference on machine learning*, PMLR, 2016, pp. 173–182.

- [4] A. Graves, A. r. Mohamed, and G. Hinton, "Speech recognition with deep recurrent neural networks," in *2013 IEEE International Conference on Acoustics, Speech and Signal Processing*, May 2013, pp. 6645–6649. DOI: 10.1109/ICASSP.2013.6638947. [Online]. Available: <http://dx.doi.org/10.1109/ICASSP.2013.6638947>.
- [5] T. Mikolov, M. Karafiát, L. Burget, J. Černocký, and S. Khudanpur, "Recurrent neural network based language model," in *Proceedings of the 11th Annual Conference of the International Speech Communication Association (INTERSPEECH 2010)*, vol. 2010, Makuhari, Chiba, JP: International Speech Communication Association, 2010, pp. 1045–1048, ISBN: 978-1-61782-123-3. [Online]. Available: <https://www.fit.vut.cz/research/publication/9362>.
- [6] C. Gao, R. Gehlhar, A. D. Ames, S.-C. Liu, and T. Delbruck, "Recurrent neural network control of a hybrid dynamical transmembrane prosthesis with EdgeDRNN accelerator," in *2020 IEEE International Conference on Robotics and Automation (ICRA)*, 2020, pp. 5460–5466. DOI: 10.1109/ICRA40945.2020.9196984.
- [7] O. Vinyals, I. Babuschkin, W. M. Czarnecki, et al., "Grandmaster level in StarCraft II using multi-agent reinforcement learning," *Nature*, vol. 575, no. 7782, pp. 350–354, 2019, ISSN: 1476-4687. DOI: 10.1038/s41586-019-1724-z. [Online]. Available: <https://doi.org/10.1038/s41586-019-1724-z>.
- [8] S. Mozaffari, O. Y. Al-Jarrah, M. Dianati, P. Jennings, and A. Mouzakitis, "Deep learning-based vehicle behavior prediction for autonomous driving applications: A review," *IEEE Transactions on Intelligent Transportation Systems*, pp. 1–15, 2020. DOI: 10.1109/TITS.2020.3012034.
- [9] M. Horowitz, "1.1 computing's energy problem (and what we can do about it)," in *2014 IEEE International Solid-State Circuits Conference Digest of Technical Papers (ISSCC)*, Feb. 2014, pp. 10–14. DOI: 10.1109/ISSCC.2014.6757323.
- [10] N. P. Jouppi, D. Hyun Yoon, M. Ashcraft, et al., "Ten lessons from three generations shaped Google's TPUv4i: Industrial product," in *2021 ACM/IEEE 48th Annual International Symposium on Computer Architecture (ISCA)*, 2021, pp. 1–14. DOI: 10.1109/ISCA52012.2021.00010.
- [11] S. Han, H. Mao, and W. J. Dally, "Deep compression: Compressing deep neural network with pruning, trained quantization and Huffman coding," in *International Conference on Learning Representations*, 2016. [Online]. Available: <http://arxiv.org/abs/1510.00149>.
- [12] S. Han, J. Kang, H. Mao, et al., "ESE: Efficient speech recognition engine with sparse LSTM on FPGA," in *Proceedings of the 2017 ACM/SIGDA International Symposium on Field-Programmable Gate Arrays*, ser. FPGA '17, Monterey, California, USA: Association for Computing Machinery, Feb. 2017, pp. 75–84, ISBN: 9781450343541. DOI: 10.1145/3020078.3021745. [Online]. Available: <https://doi.org/10.1145/3020078.3021745>.
- [13] A. N. Gomez, I. Zhang, K. Swersky, Y. Gal, and G. E. Hinton, "Targeted dropout," in *2018 CDNNRIA Workshop at the 32nd Conference on Neural Information Processing Systems*, NeurIPS, 2018. [Online]. Available: <https://openreview.net/pdf?id=HkghWSucoQ>.
- [14] W. Wen, Y. He, S. Rajbhandari, et al., "Learning intrinsic sparse structures within long short-term memory," in *International Conference on Learning Representations*, 2018. [Online]. Available: <https://openreview.net/forum?id=rk6cfrRjZ>.
- [15] S. Cao, C. Zhang, Z. Yao, et al., "Efficient and effective sparse LSTM on FPGA with bank-balanced sparsity," in *Proceedings of the 2019 ACM/SIGDA International Symposium on Field-Programmable Gate Arrays*, ser. FPGA '19, Seaside, CA, USA: ACM, 2019, pp. 63–72, ISBN: 978-1-4503-6137-8. DOI: 10.1145/3289602.3293898. [Online]. Available: <http://doi.acm.org/10.1145/3289602.3293898>.
- [16] M. Wang, Z. Wang, J. Lu, J. Lin, and Z. Wang, "E-LSTM: An efficient hardware architecture for long short-term memory," *IEEE Journal on Emerging and Selected Topics in Circuits and Systems*, vol. 9, no. 2, pp. 280–291, 2019. DOI: 10.1109/JETCAS.2019.2911739.
- [17] D. Kadedotad, S. Yin, V. Berisha, C. Chakrabarti, and J. Seo, "An 8.93 TOPS/W LSTM recurrent neural network accelerator featuring hierarchical Coarse-Grain sparsity for On-Device speech recognition," *IEEE J. Solid-State Circuits*, vol. 55, no. 7, pp. 1877–1887, Jul. 2020, ISSN: 0018-9200, 1558-173X. DOI: 10.1109/JSSC.2020.2992900. [Online]. Available: <http://dx.doi.org/10.1109/JSSC.2020.2992900>.
- [18] Z. Wang, J. Lin, and Z. Wang, "Accelerating recurrent neural networks: A memory-efficient approach," *IEEE Transactions on Very Large Scale Integration (VLSI) Systems*, vol. 25, no. 10, pp. 2763–2775, Oct. 2017, ISSN: 1063-8210. DOI: 10.1109/TVLSI.2017.2717950.

- [19] S. Wang, Z. Li, C. Ding, *et al.*, “C-LSTM: Enabling efficient LSTM using structured compression techniques on FPGAs,” in *Proceedings of the 2018 ACM/SIGDA International Symposium on Field-Programmable Gate Arrays*, ser. FPGA ’18, Monterey, CALIFORNIA, USA: ACM, 2018, pp. 11–20, ISBN: 978-1-4503-5614-5. DOI: 10.1145/3174243.3174253. [Online]. Available: <http://doi.acm.org/10.1145/3174243.3174253>.
- [20] Z. Li, C. Ding, S. Wang, *et al.*, “E-RNN: Design optimization for efficient recurrent neural networks in FPGAs,” in *2019 IEEE International Symposium on High Performance Computer Architecture (HPCA)*, 2019, pp. 69–80. DOI: 10.1109/HPCA.2019.00028.
- [21] D. Neil, J. Lee, T. Delbrück, and S. Liu, “Delta networks for optimized recurrent network computation,” in *Proceedings of the 34th International Conference on Machine Learning, ICML 2017, Sydney, NSW, Australia, 6-11 August 2017*, 2017, pp. 2584–2593. [Online]. Available: <http://proceedings.mlr.press/v70/neil17a.html>.
- [22] C. Gao, D. Neil, E. Ceolini, S.-C. Liu, and T. Delbruck, “DeltaRNN: A power-efficient recurrent neural network accelerator,” in *Proceedings of the 2018 ACM/SIGDA International Symposium on Field-Programmable Gate Arrays*, ser. FPGA ’18, Monterey, CALIFORNIA, USA: ACM, 2018, pp. 21–30, ISBN: 978-1-4503-5614-5. DOI: 10.1145/3174243.3174261. [Online]. Available: <http://doi.acm.org/10.1145/3174243.3174261>.
- [23] C. Gao, A. Rios-Navarro, X. Chen, S.-C. Liu, and T. Delbruck, “EdgeDRNN: Recurrent neural network accelerator for edge inference,” *IEEE Journal on Emerging and Selected Topics in Circuits and Systems*, vol. 10, no. 4, pp. 419–432, 2020. DOI: 10.1109/JETCAS.2020.3040300.
- [24] A. Aimar, H. Mostafa, E. Calabrese, *et al.*, “NullHop: A flexible convolutional neural network accelerator based on sparse representations of feature maps,” *IEEE Transactions on Neural Networks and Learning Systems*, vol. 30, no. 3, pp. 644–656, 2019. DOI: 10.1109/TNNLS.2018.2852335.
- [25] Q. Chen, Y. Huang, R. Sun, *et al.*, “An efficient accelerator for multiple convolutions from the sparsity perspective,” *IEEE Transactions on Very Large Scale Integration (VLSI) Systems*, vol. 28, no. 6, pp. 1540–1544, 2020. DOI: 10.1109/TVLSI.2020.2976454.
- [26] C. Xu, J. Yao, Z. Lin, *et al.*, “Alternating multi-bit quantization for recurrent neural networks,” in *International Conference on Learning Representations*, 2018. [Online]. Available: <https://openreview.net/forum?id=S19dR9x0b>.
- [27] I. S. Duff, R. G. Grimes, and J. G. Lewis, “Sparse matrix test problems,” *ACM Trans. Math. Softw.*, vol. 15, no. 1, pp. 1–14, Mar. 1989, ISSN: 0098-3500. DOI: 10.1145/62038.62043. [Online]. Available: <https://doi.org/10.1145/62038.62043>.
- [28] A. Percey, “Advantages of the Virtex-5 FPGA 6-Input LUT architecture,” *White Paper: Virtex-5 FPGAs, Xilinx WP284 (v1.0)*, 2007. [Online]. Available: https://classes.engineering.wustl.edu/cse460t/images/9/98/Xilinx_vs_Altera.pdf.
- [29] Intel, “Stratix III FPGAs vs. Xilinx Virtex-5 Devices: Architecture and Performance Comparison,” *White Paper: WP-01003-1.0*, 2006. [Online]. Available: <https://www.intel.com/content/dam/www/programmable/us/en/pdfs/literature/wp/wp-01003.pdf>.
- [30] J. S. Garofolo, L. F. Lamel, W. M. Fisher, J. G. Fiscus, D. S. Pallett, and N. L. Dahlgren, *DARPA TIMIT acoustic phonetic continuous speech corpus CDROM*, 1993.
- [31] A. Graves, S. Fernández, F. Gomez, and J. Schmidhuber, “Connectionist temporal classification: Labelling unsegmented sequence data with recurrent neural networks,” in *Proceedings of the 23rd international conference on Machine learning*, ser. ICML ’06, Pittsburgh, Pennsylvania, USA: Association for Computing Machinery, Jun. 2006, pp. 369–376, ISBN: 9781595933836. DOI: 10.1145/1143844.1143891. [Online]. Available: <https://doi.org/10.1145/1143844.1143891>.
- [32] V. Panayotov, G. Chen, D. Povey, and S. Khudanpur, “Librispeech: An asr corpus based on public domain audio books,” in *2015 IEEE International Conference on Acoustics, Speech and Signal Processing (ICASSP)*, 2015, pp. 5206–5210. DOI: 10.1109/ICASSP.2015.7178964.
- [33] M. Ravanelli, T. Parcollet, and Y. Bengio, “The Pytorch-kaldi speech recognition toolkit,” in *ICASSP 2019 - 2019 IEEE International Conference on Acoustics, Speech and Signal Processing (ICASSP)*, 2019, pp. 6465–6469. DOI: 10.1109/ICASSP.2019.8683713.
- [34] D. Povey, A. Ghoshal, G. Boulianne, *et al.*, “The kaldi speech recognition toolkit,” in *IEEE 2011 workshop on automatic speech recognition and understanding*, infoscience.epfl.ch, 2011. [Online]. Available: <https://infoscience.epfl.ch/record/192584>.
- [35] M. Gales, “Maximum likelihood linear transformations for hmm-based speech recognition,” *Computer Speech & Language*, vol. 12, no. 2, pp. 75–98, 1998, ISSN: 0885-2308. DOI: <https://doi.org/10.1006/csla.1998.0043>. [Online]. Available: <https://www.sciencedirect.com/science/article/pii/S088523089800432>.
- [36] E. Stomatias, D. Neil, M. Pfeiffer, F. Galluppi, S. B. Furber, and S.-C. Liu, “Robustness of spiking deep belief networks to noise and reduced bit precision of neuro-inspired hardware platforms,” *Frontiers in Neuroscience*, vol. 9, p. 222, 2015, ISSN: 1662-453X. DOI: 10.3389/fnins.2015.00222. [Online]. Available: <https://www.frontiersin.org/article/10.3389/fnins.2015.00222>.
- [37] N. Srivastava, G. Hinton, A. Krizhevsky, I. Sutskever, and R. Salakhutdinov, “Dropout: A simple way to prevent neural networks from overfitting,” *Journal of Machine Learning Research*, vol. 15, no. 56, pp. 1929–1958, 2014. [Online]. Available: <http://jmlr.org/papers/v15/srivastava14a.html>.
- [38] J. Frankle and M. Carbin, “The lottery ticket hypothesis: Finding sparse, trainable neural networks,” in *International Conference on Learning Representations*, 2019. [Online]. Available: <https://openreview.net/forum?id=rJl-b3RcF7>.
- [39] E. Malach, G. Yehudai, S. Shalev-Schwartz, and O. Shamir, “Proving the lottery ticket hypothesis: Pruning is all you need,” in *Proceedings of the 37th International Conference on Machine Learning*, H. D. III and A. Singh, Eds., ser. Proceedings of Machine Learning Research, vol. 119, PMLR, Jul. 2020, pp. 6682–6691. [Online]. Available: <https://proceedings.mlr.press/v119/malach20a.html>.
- [40] S. Han, J. Pool, S. Narang, *et al.*, “DSD: Dense-Sparse-Dense training for deep neural networks,” in *International Conference on Learning Representations*, 2017, Poster C4. [Online]. Available: https://openreview.net/pdf?id=HyoST_9xl.
- [41] C. Gao, S. Braun, I. Kiselev, J. Anumula, T. Delbruck, and S.-C. Liu, “Real-time speech recognition for iot purpose using a delta recurrent neural network accelerator,” in *2019 IEEE International Symposium on Circuits and Systems (ISCAS)*, 2019, pp. 1–5. DOI: 10.1109/ISCAS.2019.8702290.
- [42] H. Sak, A. Senior, and F. Beaufays, “Long short-term memory recurrent neural network architectures for large scale acoustic modeling,” in *Fifteenth Annual Conference of the International Speech Communication Association*, 2014.
- [43] Micron, *TN-ed-03: GDDR6: The next-generation graphics DRAM*. [Online]. Available: https://www.micron.com/-/media/client/global/documents/products/technical-note/dram/tned03_gddr6.pdf.
- [44] M. O’Connor, N. Chatterjee, D. Lee, *et al.*, “Fine-Grained DRAM: Energy-Efficient DRAM for extreme bandwidth systems,” in *2017 50th Annual IEEE/ACM International Symposium on Microarchitecture (MICRO)*, ieeexplore.ieee.org, Oct. 2017, pp. 41–54. [Online]. Available: <https://ieeexplore.ieee.org/abstract/document/8686544/>.



learning with emphasis on recurrent neural networks.



robotics.

Chang Gao (Member, IEEE) received the BEng degree in Electronics from University of Liverpool, Liverpool, UK and Xi’an Jiaotong-Liverpool University, Suzhou, China, and the MSc degree in analog and digital integrated circuit design from Imperial College London, London, UK. He was awarded his Doctoral degree at the Institute of Neuroinformatics, University of Zurich and ETH Zurich, Zurich, Switzerland in Dec. 2021 and is joining TU Delft as an Assistant Professor in 2022. His current research interests include computer architectures for deep

Tobi Delbruck (Fellow, IEEE) received the B.Sc. degree in physics from the University of California at San Diego, San Diego, CA, USA, in 1986, and the Ph.D. degree from the California Institute of Technology, Pasadena, CA, USA, in 1993. Since 1998, he has been with the Institute of Neuroinformatics, University of Zurich and ETH Zurich, Zürich, Switzerland, where he is a Professor of physics and electrical engineering. His group along with S.-C. Liu focuses on neuromorphic sensory processing, efficient hardware AI, and control for



Shih-Chii Liu (Fellow, IEEE) received the bachelor's degree in electrical engineering from the Massachusetts Institute of Technology, Cambridge, MA, USA, and the Ph.D. degree in the computation and neural systems program from the California Institute of Technology, Pasadena, CA, USA, in 1997. She was with various companies, including Gould American Microsystems, San Jose, CA, USA, LSI Logic, Sherman Oaks, CA, USA, and Rockwell International Research Labs, Thousand Oaks, CA, USA. She is Professor and Group Leader at the

Institute of Neuroinformatics, University of Zurich and ETH Zurich, Zürich, Switzerland.